Heliyon 5 (2019) e02416

Contents lists available at ScienceDirect

Heliyon

journal homepage: www.heliyon.com

A numerical investigation of the heat transfer characteristics of water-based mango bark nanofluid flowing in a double-pipe heat exchanger

E.J. Onyiriuka [a], O.O. Ighodaro [a], A.O. Adelaja [b,**], D.R.E. Ewim [c,d,*], S. Bhattacharyya [e]

[a] Department of Mechanical Engineering, University of Benin, PMB 1154, Benin City, Edo State, Nigeria
[b] Department of Mechanical Engineering, University of Lagos, Akoka-Yaba, Lagos, Nigeria
[c] Department of Mechanical and Aeronautical Engineering, University of Pretoria, Private Bag X20, Hatfield, Pretoria, 0028, South Africa
[d] Nigeria Atomic Energy Commission, No. 9, Kwame Nkrumah Crescent Asokoro, P.M.B., 646, Garki, Abuja, Nigeria
[e] Department of Mechanical Engineering, BITS-Pilani, Pilani Campus, Rajasthan 333 031, India

ARTICLE INFO

Keywords:
Chemical engineering
Energy
Mechanical engineering
Nanotechnology
Mixture model
Bio-nanoparticle
Double-pipe heat exchanger
Heat transfer

ABSTRACT

In this study, the heat transfer characteristics of a new class of nanofluids made from mango bark was numerically simulated and studied during turbulent flow through a double pipe heat exchanger. A range of volume fractions was considered for a particle size of 100 nm. A two-phase flow was considered using the mixture model. The mixture model governing equations of continuity, momentum, energy and volume fraction were solved using the finite-volume method. The results showed an increase of the Nusselt number by 68% for a Reynolds number of 5,000 and 45% for a Reynolds number of 13 000, and the heat transfer coefficient of the nanofluid was about twice that of the base fluid. In addition, the Nusselt number decreased by an average value of 0.76 with an increase of volume fraction by 1%. It was also found that there was a range of Reynolds numbers in which the trend of the average heat transfer coefficient of the nanofluid was completely reversed, and several plots showing zones of higher heat transfer which if taken advantage of in design will lead to higher heat transfer while avoiding other zones that have low heat transfer. It is hoped that these results will influence the thermal design of new heat exchangers.

1. Introduction

Heat exchange equipment is a device that aids the transfer of heat energy between two or more fluids that are at different temperatures. The fluids may be in direct contact or may be separated from mixing together. They are applied practically for a wide range of uses, in both heating and cooling processes in air-conditioning systems either industrial or domestic, process, and power generation [1]. Nanofluids are heat transfer fluids which usually have a higher thermal performance than other conventional fluids and have been investigated for a long time as an alternative working fluid. They are formed from the suspension of small solid particles of nanometer size in a base fluid. These solid particles are typically either metallic, non-metallic, polymeric and bio-based. This innovative fluid was introduced first at Argonne National Laboratory some decades ago by Choi [2]. Since that time, there have been remarkable and innovative investigations by researchers in various fields such as chemical engineering, medicine, transport, power generation, industrial processes, micro-sized applications, and heating and cooling processes. Although there have been numerous nanofluid-related studies, results and findings are still evolving and far from perfect. For example, an accurate correlation for the nanofluids' thermophysical properties has eluded scientists up to now and this could be due to the fact that nanofluids vary in their percentage composition of solid particles, and as the percentage increases the physics governing the nanofluids changes. Therefore, it makes it impossible to use one model to accurately capture all its physical behaviour across all percentage compositions.

For new energy-efficient heat transfer equipment, it is imperative to have compact designs, but due to the inherently low thermal conductivity of conventional fluids, achieving compact designs has been difficult [3]. However, with the development of various nanofluids, the heat transfer properties of the base fluid are increased significantly, hence the prospect of achieving compact-size heat transfer devices have risen. Before the advent of nanofluids, micrometre or even millimetre-sized particles were used but the drawbacks included blocking of pipes, corrosion of conduits and high-pressure drop when applied in practice. Furthermore, they had rheological and stability issues wherein the

* Corresponding author.
** Corresponding author.
E-mail addresses: aadelaja@unilag.edu.ng (A.O. Adelaja), daniel.ewim@up.ac.za (D.R.E. Ewim).

https://doi.org/10.1016/j.heliyon.2019.e02416
Received 12 February 2019; Received in revised form 6 May 2019; Accepted 30 August 2019

particles settled very fast from the suspension, which also meant higher costs since the settled particles would have to be replaced each time. All these drawbacks made them unsuitable for use in practical applications.

Several existing articles [3, 4, 5, 6, 7, 8, 9, 10, 11, 12, 13, 14, 15] have been published which were dedicated to the study of nanofluids and the most relevant ones are presented in this section. Wen and Ding [16] studied the thermal characteristics of γ-Al_2O_3 nanoparticles dispersed in deionized water in the laminar flow regime under a constant wall heat flux condition with particular interest on the entrance region. It was found that the local heat transfer coefficient varied with regards to Reynolds number and volume fraction. Furthermore, it was found that there was a noticeable rise in the coefficient of heat transfer in the entrance region which led to a reduction in the thermal boundary layer thickness which reduced with axial distance. They suggested a possibility of smart entrance region to harness the particularly high performance at the entrance region. Nakhjavani et al. [17] produced silver nanoparticles via green synthesis method using green tea leaves. Their cost-effective method provided condition to control the average nanoparticle size. The particles produced were characterized employing x-ray diffraction, UV visualization, scanning electron microscope images, zeta potential measurement, digital light scattering and thermal conductivity measurements. From their results, they demonstrated that the produced samples of silver nanoparticles were pure in structure, closely identical in terms of morphology and showed longer stability when dispersed in deionized water. They also showed that small particles had higher thermal and antimicrobial performance. They also stated that, since green tea leaves were used for extracting the silver nanoparticles, the method was ecofriendly. The thermal conductivity of the dispersed silver nanoparticles in deionized water was found to be higher than that of deionized water. Sarafraz et al. [18] experimentally measured and compared the thermal performance of deionized water and copper oxide water-based nanofluids at different operating conditions. Their results showed that if the applied heat flux was increased, the heat transfer coefficient increases for both of the test fluids at the distinguished heat transfer regions. Additionally, they found that by increasing the flow rate of fluid, heat transfer coefficient greatly increased at both regions. They showed that the fluid temperature at the inlet displaces the boundary between nucleate boiling and forced convection in that an increase in the inlet temperature, at lower heat fluxes leads to a dominance of nucleate mechanism. Sarafraz et al. [19] performed an experimental investigation on how the fouling formation of nanoparticles affect the thermal performance of chevron type flat plate heat exchangers with CuO/water as the working fluid. In their study, a low frequency vibration was applied to mitigate the fouling formation. They showed that fouling thermal resistance was decreased by introducing vibration into the system as well as intensified overall thermal performance of the system. Nikkhah et al. [20] experimentally studied convective boiling heat transfer coefficient of spherical CuO (II) nanoparticles dispersed in water inside a vertical heat exchanger with the influence of different operating parameters such as mass and heat fluxes, concentration and subcooling temperature on forced convection and nucleate boiling heat transfer mechanism. In their study, they found that by increasing mass and heat fluxes, the heat transfer coefficient increased significantly for both heat transfer regions. Also, an increase in the nanoparticle weight concentration leads to an increase in the heat transfer coefficient in convective heat transfer and reduces the heat transfer coefficient in nucleate boiling resulting in the formation of nanoparticle deposition on the heat surface.

Heris et al. [21] investigated the forced convective heat transfer coefficient of the Al_2O_3-water and CuO-water nanofluid under a laminar flow regime in an annular tube under a constant wall temperature boundary condition. Saturated steam flowed in the annulus to provide a constant wall temperature boundary condition. They found that the heat transfer coefficient increased as the Peclet number and volume fraction increased. The enhancement was found to be higher with Al_2O_3-water nanofluid than CuO-water nanofluid.

He et al. [22] carried out an experimental study to investigate the heat and flow characteristics of TiO_2-distilled water nanofluid flowing in a vertical pipe in both the laminar and turbulent flow regimes. They found that the convective heat transfer increased with nanoparticle concentration in both laminar and turbulent flow regimes at a given particle size and Reynolds number. Additionally, they showed that at a given nanoparticle concentration and Reynolds number, the heat transfer coefficient was not sensitive to particle size. They further stated that the effect of particle size on the coefficient of heat transfer was due to the movement of the nanoparticles. Finally, they found a negligible effect of the nanoparticles on the pressure drop.

Some numerical studies have been carried out on forced convection as well. Lemanowicz et al. [23] carried out a numerical simulation of nanofluid flow in a small diameter pipe and concluded that although one-phase simulation, as well as multiphase simulations, resulted in good agreement with the theoretical calculations and experimental results, they recommended using the multiphase model if possible. They stated that the multiphase approach allows one to investigate the behaviour of nanoparticles within the fluid and in some cases show more complete phenomena that would not be predicted by the single-phase model. Moraveji and Hejazian [24] carried out a numerical inspection based on the computational fluid dynamics (CFD) method, with a single-phase approach and suggested correlations to estimate the Nusselt number and friction factor based on dimensionless numbers and they observed that the modelling data were in good agreement with experimental data. Ahmed et al. [25] investigated the heat transfer enhancement in corrugated channels using SiO_2-water nanofluid both experimentally and numerically and found that the average Nusselt number and heat transfer enhancement increases as the nanoparticles' volume fraction increases at the expense of increased pressure drop. Ahmed et al. [26] numerically studied the heat transfer and nanofluid flow in a triangular duct with vortex generator using the two-phase model and found that considering the nanofluid as two separate phases is more reasonable than assuming the nanofluid as a homogeneous single phase. Saberi et al. [27] employed both the single-phase and two-phase mixture models to study the laminar forced convective heat transfer of alumina-water and zirconia-water nanofluid through a vertical heated tube. Comparing their results with experiment showed that the mixture model gave a better result by 8% and 5% error for alumina-water and zirconia-water nanofluids respectively. The single-phase approach gave 13% and 8% error on prediction.

Bianco et al. [28] performed a numerical investigation on turbulent nanofluid flow in a circular tube subject to constant heat flux. The result showed that as opposed to the single-phase model, the multiphase model (mixture model) was found to be more accurate.

Akbari et al. [7] numerically investigated forced convection flow in a horizontal pipe. The results showed that the thermal prediction using the two-phase model was very sensitive to the particle concentration, while both the single-phase approach and the two-phase models predicted almost identical flow fields.

Duangthongsuk and Wongwises [4] carried out an experimental study on heat transfer performance and pressure drop of TiO_2-water nanofluid flowing in a turbulent flow regime. It was found that the heat transfer coefficient of the nanofluid was higher than that of the base liquid. Furthermore, It was found that the heat transfer coefficients increased with increasing Reynolds number and particle concentration.

Bahiraei and Hangi [29] investigated the efficacy of magnetic nanofluid as a coolant in a double-pipe heat exchanger in the presence of a magnetic field using numerical tools and results showed that increasing particle size, concentration, and magnitude of the magnetic field led to a greater pressure drop and heat transfer enhancement.

Despite gain from using these nanofluids, there are tangible health and environmental issues associated with their use. Hence the use of nanofluids is limited, due to the fact that most of the commonly available nanofluids are toxic, harmful, and dangerous to the humans and animals exposed to them either by inhalation, ingestion, and penetration or otherwise and they are also harmful to the environment, as reported by

researchers [30, 31, 32, 33, 34, 35, 36, 37, 38]. Tabet et al. [30] reported the adverse effects of industrial multiwalled carbon nanotubes on human pulmonary cells. Chang et al. [33] stated the health effects of exposure to nano-TiO_2.

Additionally, environmental concerns due to use of non-biodegradable materials have been raised: researchers [32, 37] reported that there is amplified toxicological pollution on the environment due to the shape, size and chemical compositions of some of the nanotechnology products. They suggest that choosing less toxic materials will make huge positive impacts on the environment. Laboratory studies have shown that many nanoparticles, specifically those made of silver, copper, and zinc, have anti-microbial properties. While they may be useful for some medical applications, the introduction of such particles into the natural environment could pose a threat to beneficial microbial communities (bacteria, fungi, and archaea) such as those found in the soil [39]. Bio-nanoparticles which may be gotten from leaves, wood char and seeds could be environmentally friendly since humans are naturally exposed to these nanoparticles [40].

The experimental process of preparation and characterization of mango nanoparticle was thoroughly reported by Sharifpur et al. [40]. In their study, they prepared the nanofluid using a two-step method. In the first step, the nanoparticles were prepared by ball milling from mango bark and leaves that had been dried in sunlight. In the second step, the ultrasonic process was used to make the prepared nanoparticles suspend in deionized water to form the colloids; the required volume of nanoparticles was mixed with the necessary amount of water. This mixture was then subjected to an ultrasonic cavitation process for 1 h to prepare an even and stable fluid. They accessed the stability of the nanofluid and verified the stability with viscosity measurements at a constant temperature.

It is worth noting that the flow in the majority of practical applications in convective heat transfer is turbulent rather than laminar. This flow regime has a higher effectiveness of heat exchange than a laminar flow regime due to the mixing which happens on a microscopic scale with particle groups transported in a zig-zag path [1]. Hence this present study focuses on the turbulent flow condition.

The use of biomaterial nanoparticles in a base fluid under forced convection in a heat exchanger has not been addressed thoroughly in the literature. Thus, there is a gap in the literature that address the forced convection heat transfer of biomaterial nanofluid. In this study, a numerical investigation into the heat transfer characteristics of mango bark nanofluids in a double pipe heat exchanger is carried out. The nanofluid flows in the tube of a double pipe heat exchanger, cooling the hot water in the annulus in a counterflow arrangement. The geometry of Duangthongsuk and Wongwises [3] was chosen for validation purposes. Mango bark particles were used because they are clean, as the environment is naturally exposed to them. A value of 100 nm particle diameter is used in accordance with the results of Sharifpur et al. [40] and Solomon et al. [41].

Mango-bark nano-particles can be used to produce nanofluids for applications such as chemical engineering, medicine, transport, power generation, industrial processes, micro-sized applications, and heating and cooling processes. The method of preparation is a two-step method and full details can be found in Sharifpur et al. [40].

2. Theory/calculation

In this section, we present the mathematical description of the equations which govern the behaviour of the nanofluid studied with the turbulence model used alongside the heat transfer equations for the double-pipe heat exchanger.

2.1. Mixture model

The mixture model is based on a single fluid two-phase approach. Further explanation can be found in Onyiriuka et al. [13]. The dimensional relationships of governing equations of the model as in Eqs. (1), (2), (3), (4), (5), (6), (7), (8), (9), (10), (11), (12), (13), (14), (15), (16), and (17) are [42, 43, 44]:

Continuity,

$$\nabla.(\rho_m \vec{v}_m) = 0 \tag{1}$$

Momentum,

$$\nabla.(\rho_m \vec{v}_m \vec{v}_m) = -\nabla P + \nabla.(\mu_m \nabla \vec{v}_m) + \nabla.\left(\sum_{k=1}^{n} \phi_k \rho_k \vec{v}_{dr,k} \vec{v}_{dr,k}\right) \tag{2}$$

Energy,

$$\nabla.\left[\sum_{k=1}^{n} \phi_k \vec{v}_k (\rho_k H_k + P)\right] = \nabla.(k \nabla T) \tag{3}$$

And volume fraction

$$\nabla.(\phi_p \rho_p \vec{v}_m) = -\nabla.(\phi_p \rho_p \vec{v}_{dr,p}) \tag{4}$$

$$\vec{v} = \sum_{k=1}^{n} \frac{\phi_k \rho_k \vec{v}_k}{\rho} \tag{5}$$

$$\rho = \sum_{k=1}^{n} \phi_k \rho_k \tag{6}$$

$$\mu = \sum_{k=1}^{n} \phi_k \mu_k \tag{7}$$

$$k = \sum_{k=1}^{n} \phi_k k_k \tag{8}$$

H_k is the sensible enthalpy for phases.

The drift velocity ($\vec{v}_{dr,k}$) for the secondary phase is

$$\vec{v}_{dr,k} = \vec{v}_k - \vec{v}_m \tag{9}$$

The relative or slip velocity is defined as the velocity of the second phase (p) relative to the velocity of the primary phase (f):

$$\vec{v}_{pf} = \vec{v}_p - \vec{v}_f \tag{10}$$

The drift velocity related to the relative velocity becomes:

$$\vec{v}_{dr,p} = \vec{v}_{pf} - \sum_{k=1}^{n} \frac{\vec{v}_{fk} \phi_k \rho_k}{\rho_m} \tag{11}$$

Manninen et al. [45] and Naumann and Shiller [46] suggested the following equations for relative velocity $\vec{v}_{pf}$ and the drag function f_{drag} as:

$$\vec{v}_{pf} = \frac{\rho_p d_p^2}{18 \mu_m f_{drag}} \frac{\rho_p - \rho_m}{\rho_p} \vec{a} \tag{12}$$

$$f_{drag} = \begin{cases} 1 + 0.15 Re_p^{0.687} & Re_p \leq 1000 \\ 0.0183 Re_p & Re_p \geq 1000 \end{cases} \tag{13}$$

Here the acceleration is determined by

$$\vec{a} = \vec{g} - (\vec{v}_m.\nabla)\vec{v}_m \tag{14}$$

d_p represents the diameter of the nanoparticles of the secondary phases while $\vec{a}$ is the secondary phase particles' acceleration.

The solids shear viscosity is defined as the addition of collisional and kinetic parts and the optional frictional part.

Syamlal et al. [47] provide the collisional part, which is a viscosity

influence due to collisions between particles taken from the kinetic theory of granular flow.

$$\mu_{p,col} = \frac{4}{5}\phi_p \rho_p d_p g_{0,pp}(1+e_{pp})\left(\frac{\Theta_p}{\pi}\right)^{1/2}\phi_p \tag{15}$$

while for the kinetic viscosity part, the Syamlal et al. [47] model is used for the calculations and is given as:

$$\mu_{p,kin} = \frac{\phi_p d_p \rho_p \sqrt{\Theta_p \pi}}{6(3-e_{pp})}\left[1+\frac{2}{5}(1+e_{pp})(3e_{pp}-1)\phi_p g_{0,pp}\right] \tag{16}$$

and the bulk viscosity is the granular particles' resistance to compression or expansion. The model is developed from the kinetic theory of granular flow based on Lun et al. [48].

$$\lambda_p = \frac{4}{3}\phi_p \rho_p d_p g_{0,pp}(1+e_{pp})\left(\frac{\Theta_p}{\pi}\right)^{1/2} \tag{17}$$

wherein Eqs. (15), (16), and (17) $g_{0,pp}$ is the radial distribution function, Θ_p is the granular temperature and e_{pp} is the restitution coefficient and λ_p is the bulk viscosity.

2.2. Turbulence modelling

The realizable $\kappa-\varepsilon$ turbulent model was suggested by Shih et al. [49]. The equations for the turbulent kinetic (κ) and dissipation of turbulent kinetic energy (ε) used in the realizable $\kappa-\varepsilon$ turbulent model are defined in Eqs. (18), (19), (20), and (21) as:

$$div(\rho\kappa\vec{v}) = div\left\{\left(\mu+\frac{\mu_t}{\sigma_k}\right)grad\,\kappa\right\} + G_k - \rho\varepsilon \tag{18}$$

$$div(\rho\varepsilon\vec{v}) = div\left\{\left(\mu+\frac{\mu_t}{\sigma_k}\right)grad\,\varepsilon\right\} + \rho C_1 S_\varepsilon - \rho C_2\frac{\varepsilon^2}{\kappa+\sqrt{v\varepsilon}} \tag{19}$$

Here,

$C_1 = max\left[0.43, \frac{\eta}{\eta+5}\right]$, $G_k = \mu_t S^2$, $\eta = S\frac{\kappa}{\varepsilon}$ and $S = \sqrt{2S_{ij}S_{ij}}$.

From Eq. (18), G_k symbolizes the generation of turbulent kinetic energy due to the mean velocity gradients. Here, S is the modulus of the mean rate-of-strain tensor, σ_κ and σ_ε represents the effective Prandtl numbers for the turbulent kinetic energy and the rate of dissipation respectively.

Hence, μ_t is modeled as:

$$\mu_t = \frac{\rho\kappa^2}{\varepsilon}\left(A_0 + A_s\frac{\kappa U^*}{\varepsilon}\right)^{-1} \tag{20}$$

Here, A_0 and A_s are the model constants given as $A_0 = 4.04$ and $A_s = \sqrt{6}cos\phi$ respectively with

$$\phi = \frac{1}{3}cos^{-1}\sqrt{6}W,\quad U^* = \sqrt{S_{ij}S_{ij}+\tilde{\Omega}_{ij}\tilde{\Omega}_{ij}},\quad \tilde{\Omega}_{ij} = \tilde{\Omega}_{ij} - 3\varepsilon_{ijk}\omega_k \quad \text{and} \quad W = \frac{S_{ij}S_{jk}S_{ki}}{\tilde{S}^3} \tag{21}$$

Here, $\tilde{\Omega}_{ij}$ is the average rate of rotation tensor with the angular velocity ω_k. In Eqs. (19) and (20), the model constants are $C_1 = 1.44$, $C_2 = 1.9$, $\sigma_\kappa = 1.0$ and $\sigma_\varepsilon = 1.2$

2.3. Heat transfer equations

The heat transfer rate of the heating fluid is given in Eq. (22) as [1]:

$$Q_{hw} = \dot{m}_{hw} Cp_{hw}(T_{in} - T_{out})_{hw} \tag{22}$$

Here, Q_{hw} represents the heat transfer rate of the hot water, $\dot{m}_{hw}$ represents the mass flow rate of the hot water, while the heat transfer rate into the nanofluid is evaluated in Eq. (23) as [1]:

$$Q_{nf} = \dot{m}_{nf} Cp_{nf}(T_{out} - T_{in})_{nf} \tag{23}$$

Here, Q_{nf} is the heat transfer rate of the nanofluid and $\dot{m}_{nf}$ is the mass flow rate of the nanofluid.

The average heat transfer rate between the hot water and the nanofluid is represented by Q_{ave} and is given in Eq. (24) as [3]:

$$Q_{ave} = \frac{Q_{hw}+Q_{nf}}{2} \tag{24}$$

The heat transfer properties, Nu_{nf} and h_{nf} of the nanofluids are estimated in Eqs. (25) and (26) [3]:

$$h_{nf} = \frac{q_{ave}}{T_w - T_{nf}} \tag{25}$$

$$Nu_{nf} = \frac{h_{nf}D}{k_{nf}} \tag{26}$$

The logarithmic mean temperature difference (LMTD) is calculated in Eq. (27) [1]:

$$LMTD = \frac{\Delta T_1 - \Delta T_2}{\ln\left(\frac{\Delta T_1}{\Delta T_2}\right)} \tag{27}$$

where ΔT_1 and ΔT_2 represent the variation in temperature between the water and nanoparticle at the entrance and exit of the heat exchanger [1].

The heat exchanger effectiveness is calculated by Eq. (28) [1]:

$$\text{Effectiveness} = \frac{Actual\ Heat\ Transfer\ Rate}{Maximum\ Possible\ Heat\ Transfer\ Rate} \tag{28}$$

3. Methods

3.1. The thermophysical properties of the nanofluid

Several models and correlations exist that can be used to calculate properties like density, heat capacity, thermal conductivity, and viscosity, as proposed and reported by researchers [7, 13, 28, 50, 51, 52, 53]. However, issues of estimating the and viscosity and thermal conductivity accurately still exist [13, 54]. Table 1 shows the properties of the base fluid and nanoparticles at 288 K [41, 55].

3.2. Nanofluid density and specific heat

The following equations are employed to calculate the density and heat capacity of the nanofluid in Eqs. (29) and (30) as.

$$\rho_{nf} = (1-\phi)\rho_{bf} + \phi\rho_p \tag{29}$$

$$\rho_{nf}Cp_{nf} = (1-\phi)(Cp_{bf}\rho_{bf}) + \phi(Cp_p\rho_p) \tag{30}$$

3.3. Nanofluid dynamic viscosity

For the constant property assumption, the effective viscosity depends only on the volume fraction ϕ and is given according to [56] in Eq. (31) as:

Table 1
Physical properties of the base fluid and nanoparticles at 288 K [41, 55].

Properties	Water	Mango-bark
$Cp(J/kgK)$	4 186	2 310
$k(W/mK)$	0.595	0.173
$\rho(kg/m^3)$	999	1 589
$\mu(kg/ms)$	0.001136	–

$$\mu_{nf} = \frac{\mu_{bf}}{(1 - 2.5\phi)} \tag{31}$$

3.4. Nanofluid thermal conductivity

For the constant properties assumption, the effective thermal conductivity is calculated by Eq. (32) [57]

$$k_{nf} = k_{bf}\left[1 + \left[0.0193 + 0.00383\left(\frac{\rho_p}{\rho_{bf}}\right)\right]\sqrt{\phi\frac{d_p}{d_{bf}}}\right] \tag{32}$$

where d_{bf} is the effective size of carrier fluid molecule.

3.5. Geometric configuration and set-up

A two-dimensional axisymmetric geometry was considered for the double-pipe heat exchanger (Fig. 1a). The geometry was a counterflow horizontal double tube heat exchanger 1.5 m long, with nanofluid flowing inside the tube and the water flowing in the annulus. The inner tube was made from a smooth copper tube with an inner and outer diameter of 8.13 mm and 9.53 mm respectively. On the hand, the outer tube was made from a PVC tube with an internal diameter of 27.8 mm.

3.6. Grid sensitivity

For the purpose of justifying the correctness and the stability of the numerical results, a number of computations have been executed to determine the total number of grid points that will give accurate and acceptable results that are fit to define the flow and thermal field in the double-pipe geometry considered. The grid sensitivity investigation is done by changing the total number of grid spreading in both radial and axial directions. In a test case of water (the base fluid) with Re = 6 100, several combinations of grids were studied to justify that the numerical results do not change further with the change of grid distribution. This step is called the grid independence study or grid sensitivity analysis. The grid distributions studied and their metrics are Mesh 1 = 9 × 1 000 (minimum orthogonal quality of 0.9 and maximum aspect ratio of 2.1), Mesh 2 = 15 × 1 500 (minimum orthogonal quality of 0.8 and maximum aspect ratio of 4.0), Mesh 3 = 28 × 3000 (minimum orthogonal quality of 0.76 and maximum aspect ratio of 4.0), Mesh 4 = 38 × 4000 (minimum orthogonal quality of 0.89 and maximum aspect ratio of 5.1).

Fig. 2 depicts the variation of the heat transfer coefficient along the length of the double-pipe heat exchanger. It can be observed that there is only a 0.2% maximum deviation of Mesh 3 from Mesh 4. While the other two grid distribution (Mesh 1 and Mesh 2) deviates significantly. Furthermore, Fig. 3a is presented for Re = 5 000 to show the

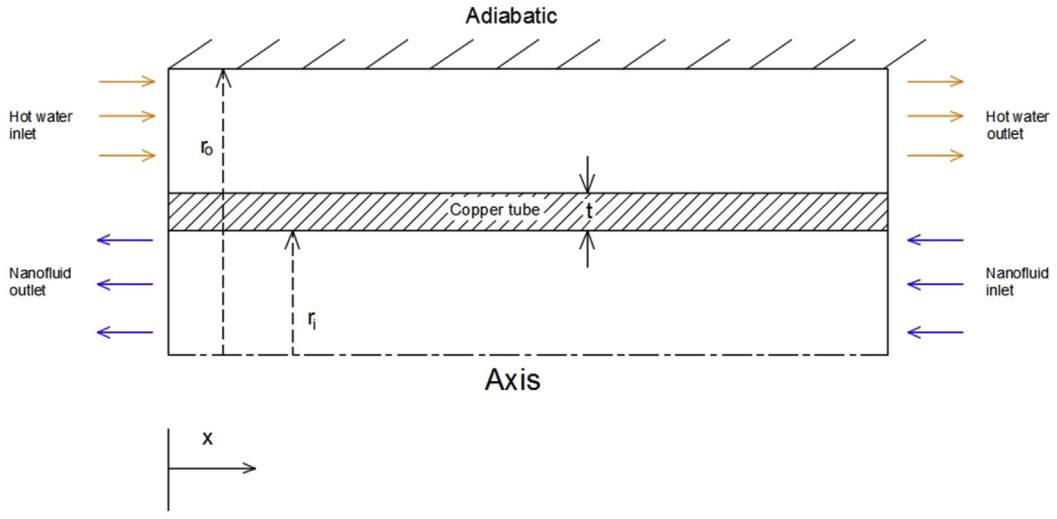

(a)

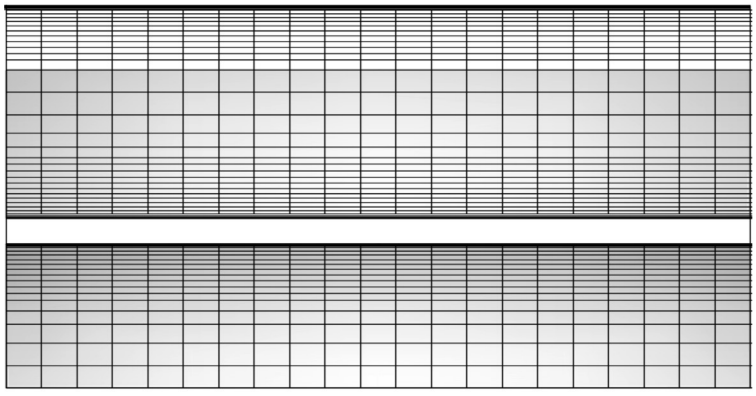

(b)

Fig. 1. Domain (a) Geometrical configuration for the present study (b). Mesh for the present study.

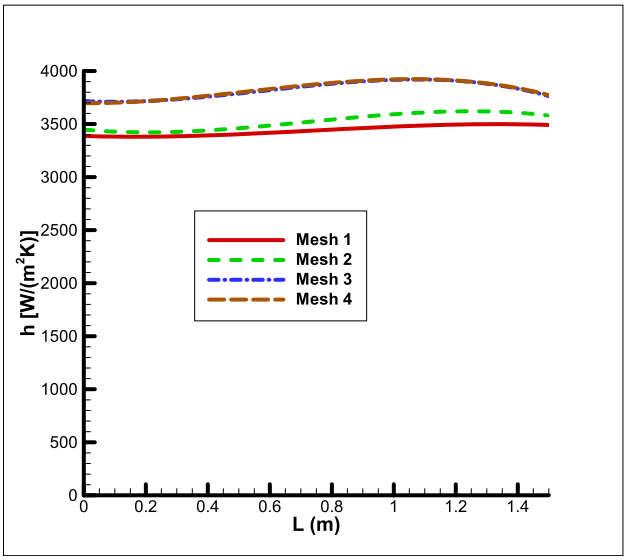

Fig. 2. Comparison of grid distributions for heat transfer coefficient along the length of the heat exchanger at $Re = 6100$.

variation of temperature along the inner radius at $x = 1.0$ m, Fig. 3b is presented again for $Re = 5000$ to show the variation of velocity along the inner radius at $x = 1.0$ m and Fig. 3c is presented for $Re = 5\,000$ to show the variation of turbulent kinetic energy profiles along the inner radius at a location $x = 1.0$ m. This is chosen since at that location both flow and thermal variables remain unchanged (*fully developed turbulent flow*). It can be seen that Mesh 3 and Mesh 4 generate the most reasonable results in the figures (Fig. 3) and that due to the number of elements in the various meshes, there is a variation in numerical solution and the differences found among Mesh 3 and Mesh 4 results are insignificant. Hence the grid distribution selected for the present computation is Mesh 3 as shown in Fig. 1b. It consisted of 28 elements in the radial direction and 3000 elements in the axial direction in order to save computation resources and avoid any inconsistencies in the numerical results. Additionally, the meshes were refined at locations close to the walls so that large variation of flow and thermal field behaviour near the wall are captured as shown in Fig. 1b. The aforementioned phenomenon is captured in the number of inflation layers of which its value in this study is 12.

4. Results

4.1. Validation of present numerical results

To ensure that we have solved the right equations we carried out this validation step for water and TiO_2 nanofluid.

4.1.1. Water

A plot for the variation of Nusselt number with Reynolds number for water is obtained from the present study and this plot is superimposed over the results from Gnielinski's equation (Fig. 4). A maximum deviation of 5.4% and an average deviation of 4.1% was observed. This shows a very good agreement with Gnielinski's correlation [58]. The variation can be attributed to near wall mesh distribution and temperature

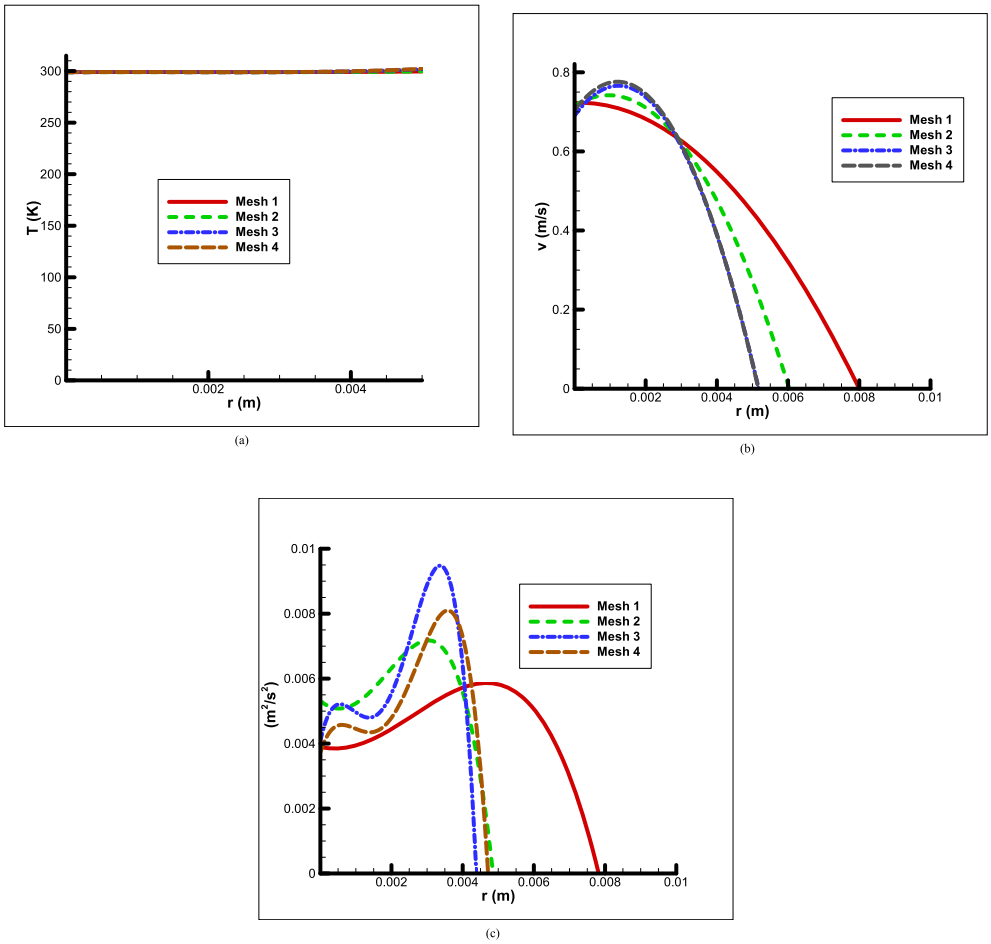

Fig. 3. Grid sensitivity (a) Comparison of grid distributions for radial temperature at $x = 1.0$ m and Re = 5000. (b) Comparison of grid distributions for radial velocity at $x = 1.0$ m and $Re = 5000$. (c) Comparison of grid distributions for radial turbulent kinetic energy at $x = 1.0$ m and Re = 5000.

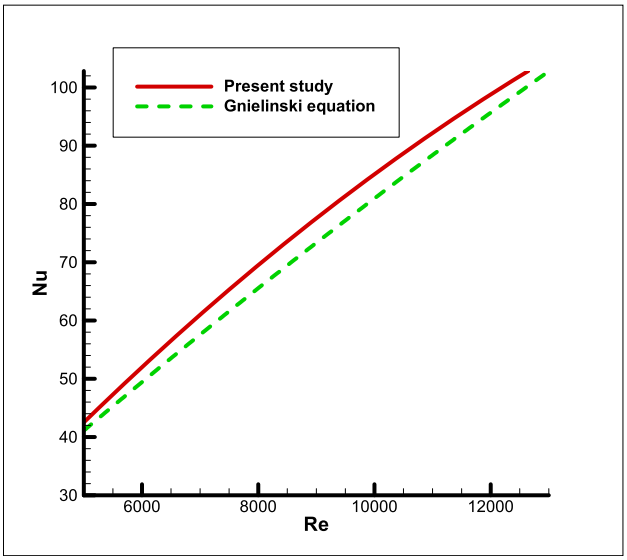

Fig. 4. Comparison between the present study and Gnielinski equation [48].

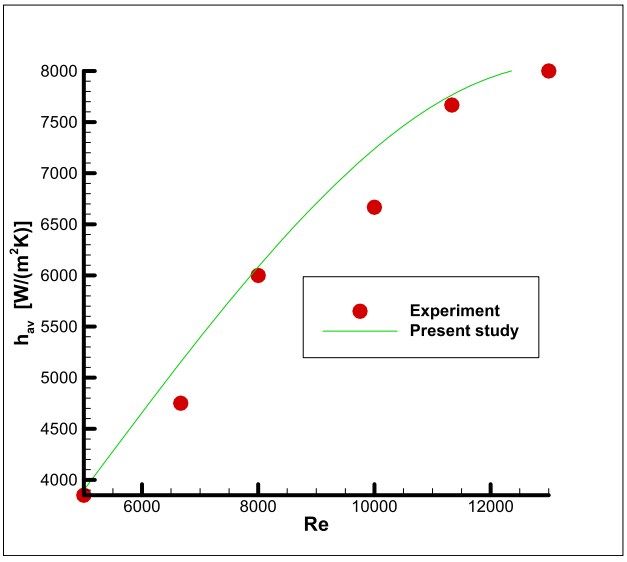

Fig. 5. Comparison of the present study with experiment for TiO_2-water nanofluid of $\phi = 0.2\%$ and $d_p = 21\ nm$.

gradient at the wall and the accuracy is problem-specific.

4.1.2. TiO_2-water nanofluid

We can satisfactorily say from the comparisons above that we have solved the right equations since our computational model is producing the correct results. Our computational model was then tested for nanofluid. We tested TiO_2-water in the inner tube of the double-pipe heat exchanger for several Reynolds numbers. The comparison (Fig. 5) is done between this study and experimental data of [3] using their experimental set-up as boundary conditions: $V_h = 0.09334\ m/s$, $t_h = 40\ ^0C$, $t_{nf} = 25\ ^0C$ with $\phi = 0.2\%$ and $d_p = 21\ nm$ for the TiO_2 nanofluid. A maximum deviation of 5% can be observed which is within good accuracy and shows good agreement with experiments.

5. Results and discussion

Results presented henceforth for nanofluid refers to water-based mango bark nanofluids of particle size of $d_p = 100\ nm$.

Fig. 6 show a comparison of dimensionless radial velocity profiles for water along the tube radius at different axial locations for $Re = 8\,333$. The hydrodynamic entry length is given by $L_{h,\ turbulent} = 1.359D\,Re_D^{\frac{1}{4}}$, which results to $x = 0.1$ m from the inlet section. It can be deduced that the flow developed quite early. This indeed is a characteristic of turbulent flow and it is due to the intense mixing during the random fluctuations which overshadows the effects of momentum and heat diffusion. Also, the hydrodynamic and thermal entry lengths are about the same size not dependent of the Prandtl number.

Fig. 7 shows the comparison of the dimensionless radial velocity profiles for nanofluid ($\phi = 0.2\%$) along the radius of the tube at different axial locations for $Re = 8\,333$. The hydrodynamic entry length is also given by $L_{h,\ turbulent} = 1.359D\,Re_D^{\frac{1}{4}}$ which results to $x = 0.1$ m from the inlet section and it is dependent on the Reynolds number, which is the same for both water and nanofluid, hence water and nanofluid have the same $L_{h,\ turbulent}\ (0.1\ m)$. Furthermore, from the expression for $L_{h,\ turbulent}$ it can be seen that the dependence of $L_{h,\ turbulent}$ on Reynolds number is very small and the flow developed very quickly, like in the case of water in the tube. The reason for this is similar to the discussion on water in Fig. 6. In addition to that discussion, the thermophysical properties (specific heat, viscosity, and density) of the two fluids (water and nanofluid) are however different. The effect due to Reynolds number being small (to the one-fourth power) makes these differences trivial.

Fig. 8 shows a plot comparing the dimensionless radial velocity profile of both water and nanofluid at $x = 0.18$ m (sufficiently large to ensure fully developed flow) for $Re = 8\,333$. It can be seen that the nanofluid radial velocity profile coincides with that of water. This is because it is independent of the volume fraction of the particles added. It must be noted here that the axial velocity profile for the nanofluid increases with an increase in volume fraction for the same Reynolds number; this is because the Reynolds number depends on the density and viscosity of the fluid of which these two properties are directly proportional to the nanoparticle volume fraction. Hence for different nanofluid volume fractions, the average velocities would be different to keep the Reynolds number steady. Furthermore, as nanoparticle concentration increases, the viscosity is enhanced at a substantially faster rate compared to the density.

Fig. 9 shows that the centerline velocity for water and nanofluid coincides at the entrance region (counterflow). There is an overshoot of the centerline velocity by 0.02 m/s which settles quickly after 0.1 m (the entrance length). This agrees with the entry length of turbulent flow theory, which is due to intense mixing in the radial direction and eddy

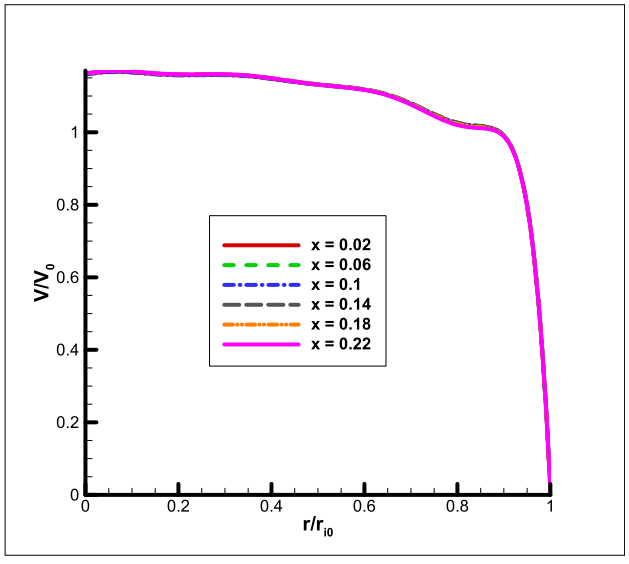

Fig. 6. Comparison of dimensionless radial velocity profiles for water at different axial locations and $Re = 8333$.

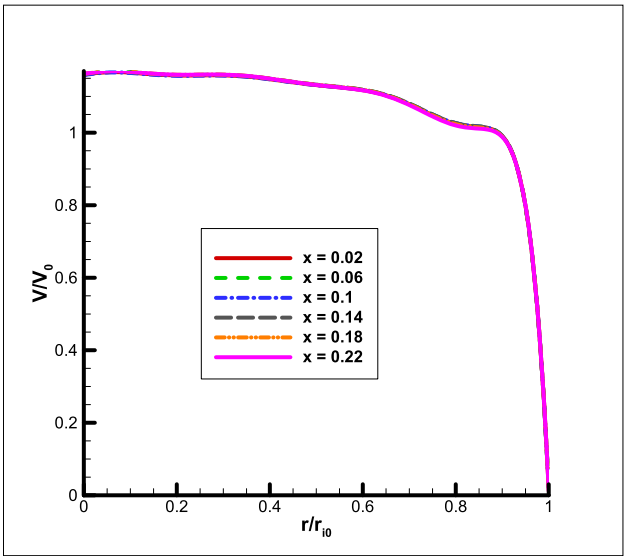

Fig. 7. Comparison of dimensionless radial velocity profiles for nanofluid at different axial locations and $Re = 8333$.

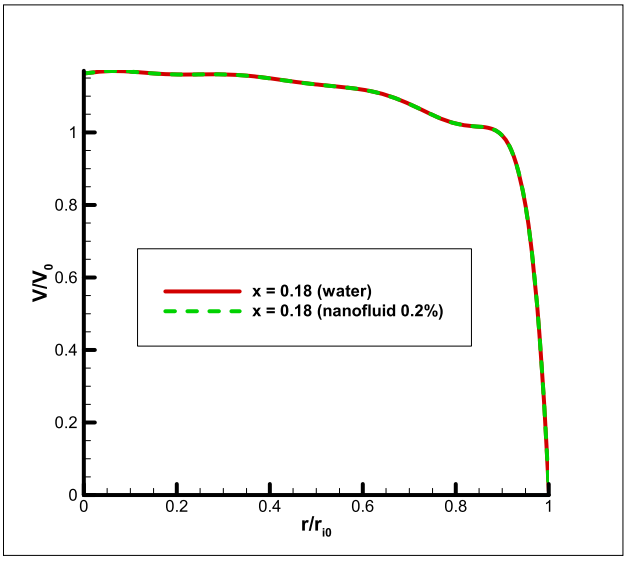

Fig. 8. Comparison of water and nanofluid dimensionless radial velocity profiles at $x = 0.18$ and $Re = 8333$.

motion. The velocity distribution remains unchanged in the fully developed region, as can be seen in the figure, and it depends on the geometry of the conduit and also the fluid and flow properties. In addition, the velocity which is along the centerline is called the maximum velocity and the deviation from it is called the velocity defect. According to the velocity defect law, the normalized velocity distribution in the core region of turbulent flow in a pipe is independent of the viscosity of the fluid but depends on the distance from the centreline. This is not surprising since the eddy motion is dominant in this region, and the effect of fluid viscosity is negligible. The characteristics of flow in the viscous sublayer are very important as they determine flow in the rest of the pipe.

The centerline temperature profile for water and nanofluid is presented in Fig. 10. Both profiles increase with length (counterflow) as they are heated by the hot fluid as they flow. The present set-up led to a temperature rise of 2.75 K at the centerline for both fluids and it is worth noting that the temperature distribution in the thermally fully developed region may change with x in the direction of flow. This differs from the velocity distribution. The temperature profile can vary at various parts of the tube in the developed region, and it normally does. However, the dimensionless temperature distribution is constant in the thermally developed region when the temperature or heat transfer rate per unit area at the tube surface remains the same. The trend in Fig. 10 shows an almost linear increase in temperature of the cold fluid with length in the flow direction as it gains temperature from cooling the hot fluid and this trend is due to the fact that the heat flux is a linear function of the change in temperature and the length of the pipe while taking the thermal conductivity of the fluid into consideration.

The juxtaposition of the dimensionless temperature profiles for (a) $\phi = 0\%$ (b) $\phi = 0.2\%$ at several tube locations is presented in Fig. 11a and b respectively. It is evident from the figure that dimensionless temperature profiles for water and nanofluid do not change after $x = 0.1$ m, hence a thermally developed flow is observed after that point. However, due to wall effects, there are variations at the wall. Furthermore, we saw from Figs. 6 and 7 that both flow profiles are also hydrodynamically developed. We can safely infer fully developed flow from these two observations. Hence the heat transfer coefficient should remain constant in this region since velocity and normalized temperature distributions do

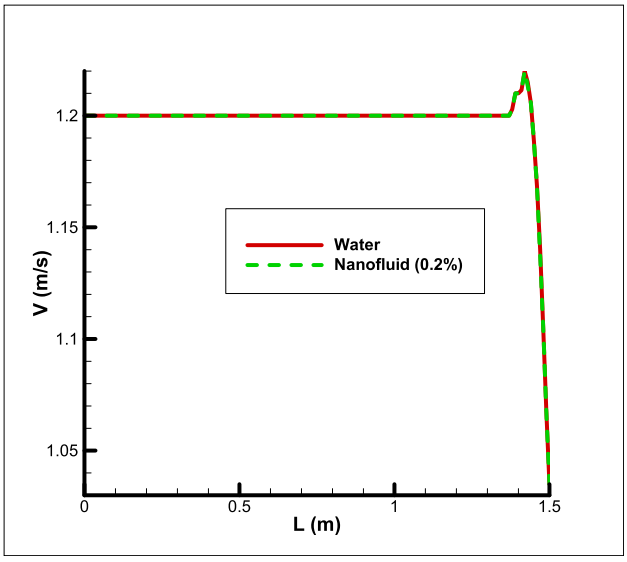

Fig. 9. Comparison of velocity along the centerline for water and nanofluid.

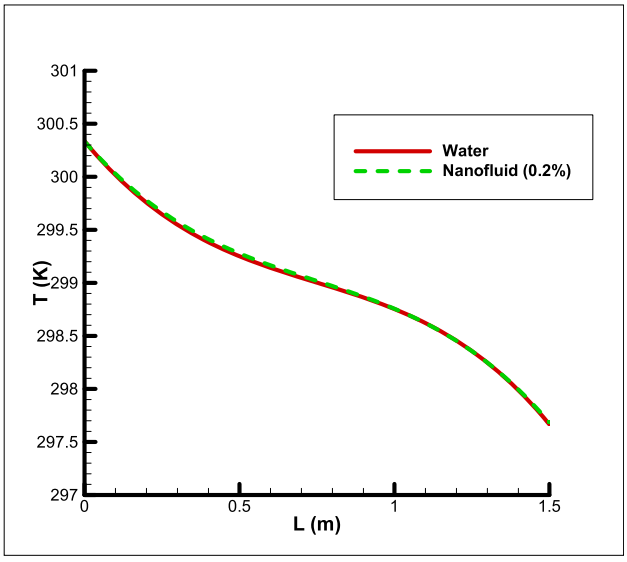

Fig. 10. Comparison of temperature along the centerline for water and nanofluid.

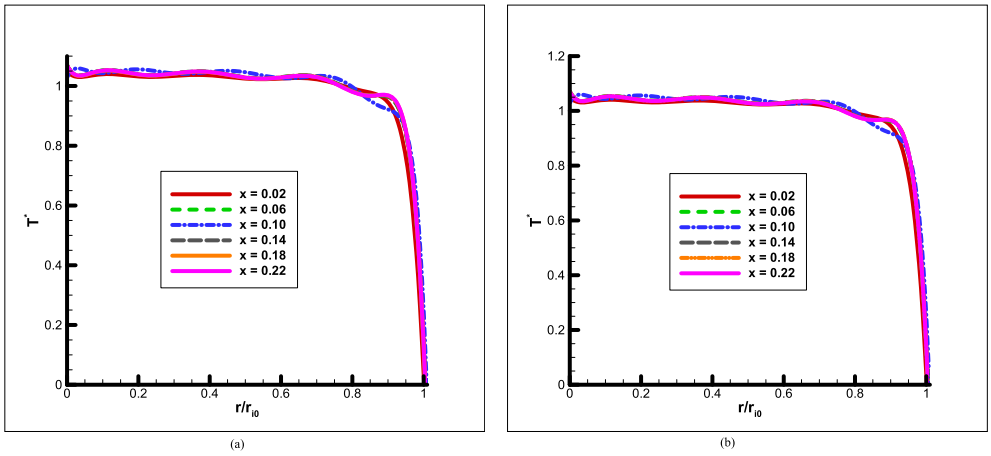

Fig. 11. Comparison of dimensionless temperature profiles for (a) $\phi = 0\%$ (b) $\phi = 0.2\%$.

not change in the flow direction. It should also be noted here that since the Prandtl number increase with volume fraction, the resulting thermal length increase with volume fraction, hence the region is pushed back as volume fraction increases. Furthermore, the quickly thermally developed flow is due to the flow being turbulent, which is characterized by vigorous mixing during random fluctuations that obliterates the effect of momentum and heat diffusion; hence the hydrodynamic and thermal entry length are very short and about the same size.

From the plot of Nusselt number against dimensionless length for water and nanofluid at $Re = 8\ 333$ (Fig. 12), an almost constant Nusselt number in the fully developed region is observed for both water and nanofluid as at the fully developed region (i.e. where the thermal and hydrodynamic boundary layers are fully developed) the thermal and flow behaviour no longer change. Additionally, it can be seen that the nanofluid has a more effective convection than water. This is due to the particles added to the water which make heat flow more effective.

Fig. 13 shows the effect of volume fraction on the Nusselt number. It can be observed from the plot that the Nusselt number drops with an increase in volume fraction (for an increase of volume fraction by 1% there is an average drop of Nusselt number by 0.76) and also no dome shape was observed in the range of the volume fractions (0.2–6%) studied. The decrease of Nusselt number with volume fraction resulted from the fact that the thermal conductivity of the fluid increases with volume fraction and since the Nusselt number and thermal conductivity are inversely related, the Nusselt number decreases as thermal conductivity increases. Furthermore, the heat transfer coefficient increases with volume fraction since the thermal conductivity of the nanofluid increases with volume fraction. It should be noted that the heat transfer coefficient is the rate of heat transfer between a solid surface (tube wall) and a fluid per unit temperature difference. So, the higher the heat transfer coefficient, the higher the heat rate: this is good for heat exchanger design, while the higher the *Nu,* the more potent, the convection. The average Nusselt number of pure water, that is, when the volume fraction is zero was 43.5 which was much lower than that of the nanofluid as can be seen in Fig. 13, where the lowest average Nusselt number was 68.8.

The Nusselt number can be seen not only to increase with Reynolds number in both fluids, as seen in Fig. 14 (for a $Re = 5\ 000$, there was a 58% increase of Nusselt number, while for $Re = 13\ 000$ there was a 45% increase), but at a lower Reynolds number the percentage increase of the Nusselt number is higher, while this increase decreases as the Reynolds number is increased. These observations are due to the fact that the Nusselt number is a strong function of the Reynolds number and bears a direct proportionality in variation: as the Reynolds number increases the Nusselt number also increases, and this relationship is an almost linear one. Also, as the Reynolds number increases, the effect of the nanoparticles is reduced, hence the decrease of the enhancement of heat transfer due to the nanoparticle addition. Furthermore, the Nusselt

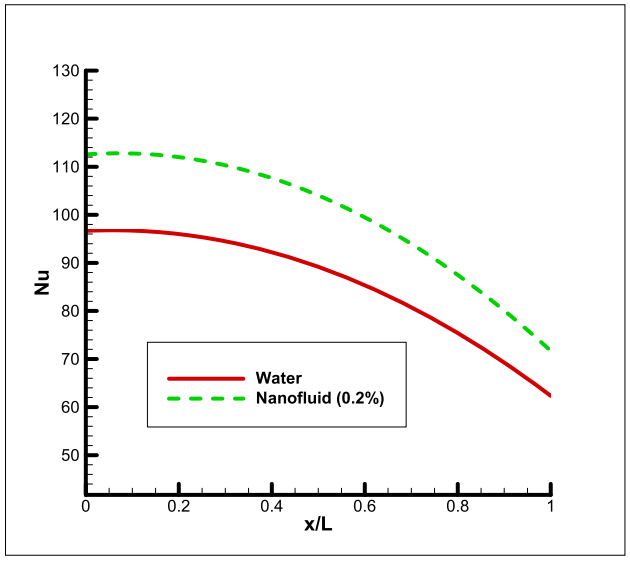

Fig. 12. Nusselt number variation with dimensionless length for water and nanofluid.

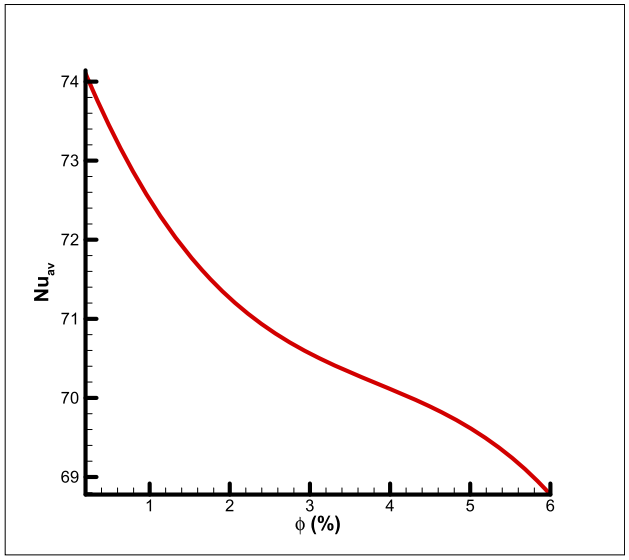

Fig. 13. Variation of Nusselt number with volume fraction.

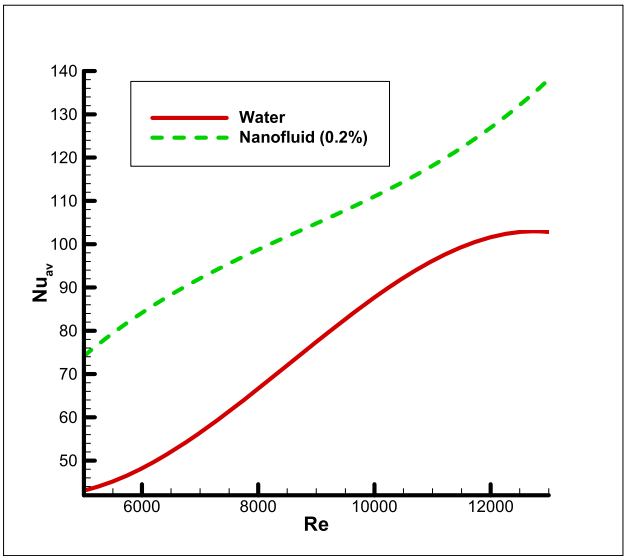

Fig. 14. Variation of Nusselt number with Reynolds number for water and nanofluid.

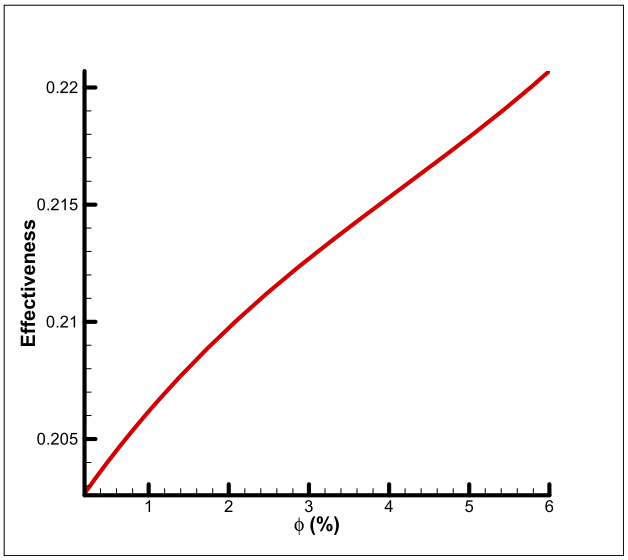

Fig. 16. Effectiveness variation with volume fraction for nanofluid.

number in the case of nanofluid was seen to be higher than that of the case of water; this was because the added particles which increased heat transfer performance and viscosity which resulted in more effective convection for nanofluid than for water.

The average heat transfer coefficient ratio, which is the ratio of the heat transfer coefficient of the nanofluids to the heat transfer coefficient of the base fluid, is plotted against the Reynolds number in Fig. 15. It is clearly seen that the ratio has its maximum value at the lowest Reynolds number. It is also clear from Fig. 15 that the nanofluid heat transfer coefficient is almost twice that of the base fluid. The decreasing trend with Reynolds number is due to the cancelling out of eddies due to particle random motion. This is similar to the trend discussed in Fig. 14. However, the lowest nanofluid average heat transfer coefficient is 1.3 times that of the base fluid.

Fig. 16 shows the plot of effectiveness with volume fraction. It is observed that the effectiveness increases with volume fraction, an overall increase of 0.019 of effectiveness over 0–6% volume fraction range, and this is because of the increase of thermal conductivity with volume fraction which leads to increased heat conduction with volume fraction. However, caution must be stated here: just because a heat exchanger has high effectiveness and a certain flow condition does not mean it will have a higher heat transfer rate than some other low-effectiveness condition.

A plot of effectiveness with Reynolds number is shown in Fig. 17. Dome shape is observed for both fluids, showing that there exists a range of Reynolds numbers (7 000 – 10 000) where the effectiveness is least; this is because the effectiveness and the Reynolds numbers are related by a polynomial function. Also, nanofluid has a higher effectiveness value than water; this is because the heat transfer rate of nanofluid is higher than that of water due to an increase of thermal conductivity because of the added particles, hence higher heat exchanger effectiveness. High effectiveness values correspond to a small temperature difference between the hot and cold fluid, while a high heat transfer rate results from a large change in temperature. In a thermodynamic sense, higher effectiveness means a reduced value of the thermodynamic irreversibility and a smaller entropy generation. In other to get both high heat transfer and high effectiveness, the product of the surface area and overall heat transfer coefficient must increase. In addition, the heat transfer rate increases with nanoparticle volume fraction as opposed to the Nusselt number in Fig. 13. The effectiveness, therefore, represents the

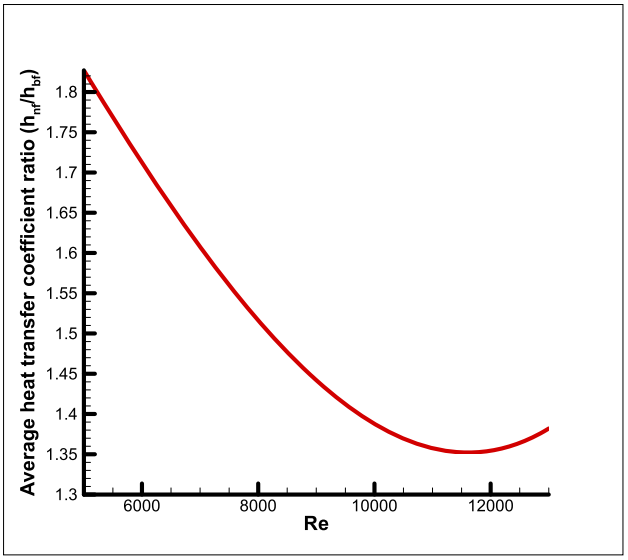

Fig. 15. Average heat transfer coefficient ratio for nanofluid ($\phi = 0.2\%$).

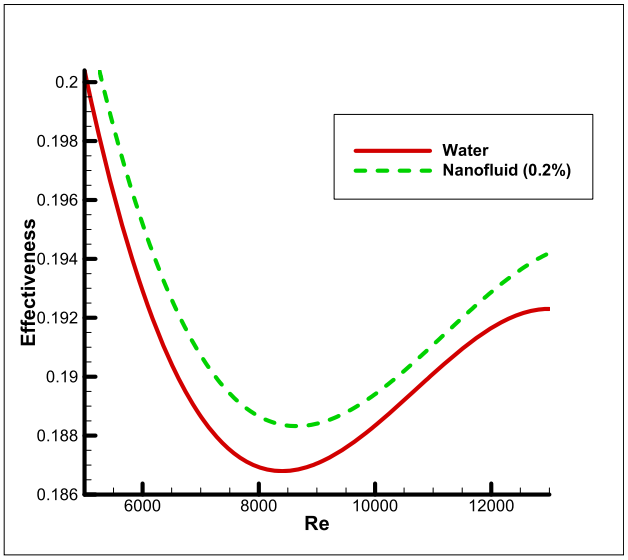

Fig. 17. Effectiveness variation with Reynolds number for water and nanofluid.

thermodynamic performance of the heat exchanger.

The *LMTD* is plotted for various volume fractions in Fig. 18 and it is found to decrease with volume fraction, a similar trend with the Nusselt number and it is also due to the increase of thermal conductivity with volume fraction. It varied by a value of about 0.13 throughout the range of volume fractions studied.

Fig. 19 shows that the *LMTD* of the nanofluid is lower than water for all Reynolds numbers. This is again due to the increase of thermal conductivity with volume fraction as discussed in Fig. 18. However, the profile for water and nanofluid for the *LMTD* plot are similar in trends and vary over the range of Reynolds numbers studied; the range of *LMTD* varies from 11.71 to 12.21, which is a difference of 0.5, while the water has a higher *LMTD* of 0.03 than the nanofluid. We can see a difference in *LMTD* of the two fluids and a range of variation with Reynolds number.

Fig. 20 shows the average heat transfer coefficient against the Reynolds number with different nanofluid temperatures at a hot water flow rate and temperature of 0.14 m/s and 45 °C respectively. The effect of nanofluid temperature is seen at higher Reynolds numbers. Furthermore, the heat transfer coefficient is greater for a lower nanofluid temperature than for a higher temperature because an increase in nanofluid

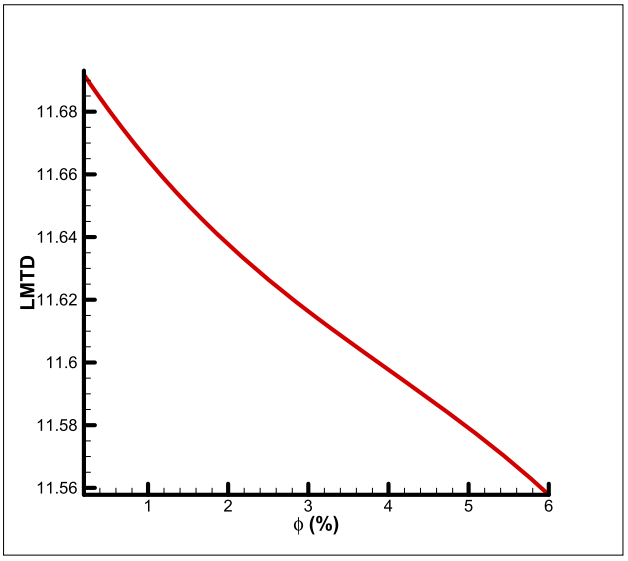

Fig. 18. *LMTD* variation with volume fraction.

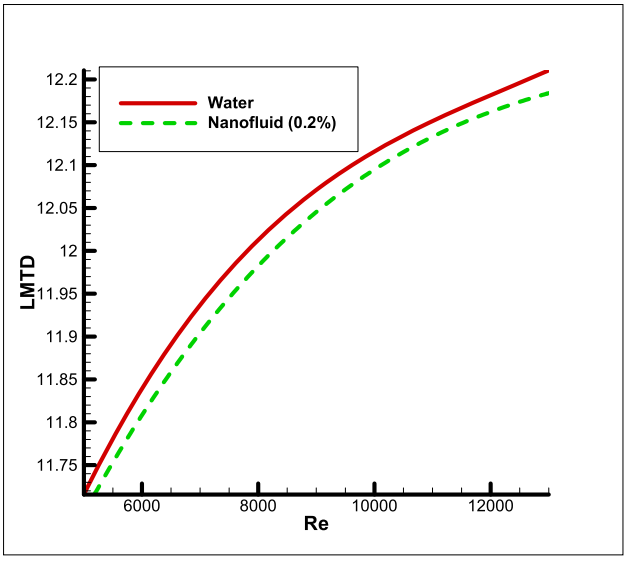

Fig. 19. Variation of *LMTD* with Re for water and nanofluid.

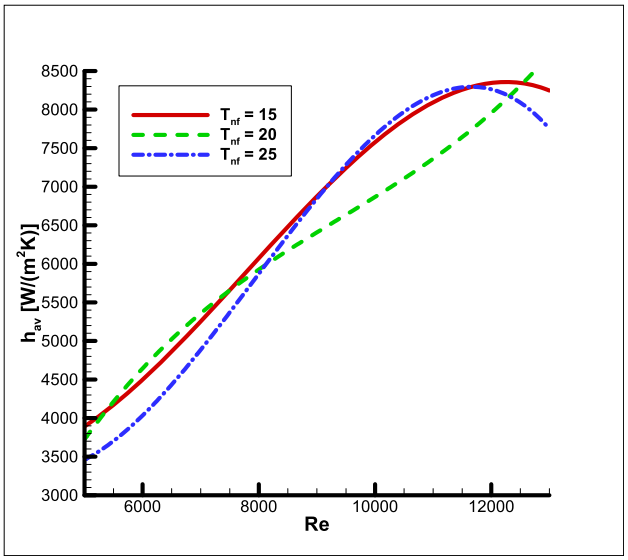

Fig. 20. Average heat transfer coefficient as a function of Reynolds number with different nanofluid temperatures.

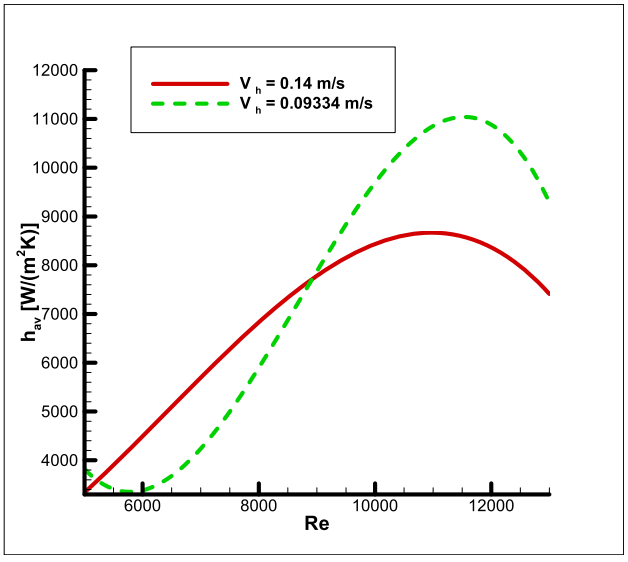

Fig. 21. Average heat transfer coefficient as a function of Reynolds number with different hot water flow rates.

temperature leads to an increase in heat transfer rate, which leads to higher heat transfer coefficient [3]. However, in this study, it was found that at (Re = 8 000) where what exists on the left to point is exactly the opposite of what is to the right of the same point. This observed behavior is due to the polynomial relationship of the Reynolds number with the effectiveness of the heat exchanger and there exists an optimal Reynolds number in the design of the heat exchanger to exploit high thermal performance; this design point could be used to design high-performing heat exchangers.

Fig. 21 shows the average heat transfer coefficient as a function of Reynolds number with different hot water flow rates, at a hot water temperature of 40 °C and nanofluid temperature of 15 °C. It is clear that the average coefficient of heat transfer of the nanofluid increases is directly proportional to the hot water flow rate until after a *Re* of 9 000 where the converse holds. This is also as a result of the polynomial relationship of Reynolds numbers and effectiveness of a heat exchanger as discussed in Fig. 20.

Fig. 22 shows the average heat transfer coefficient as a function of

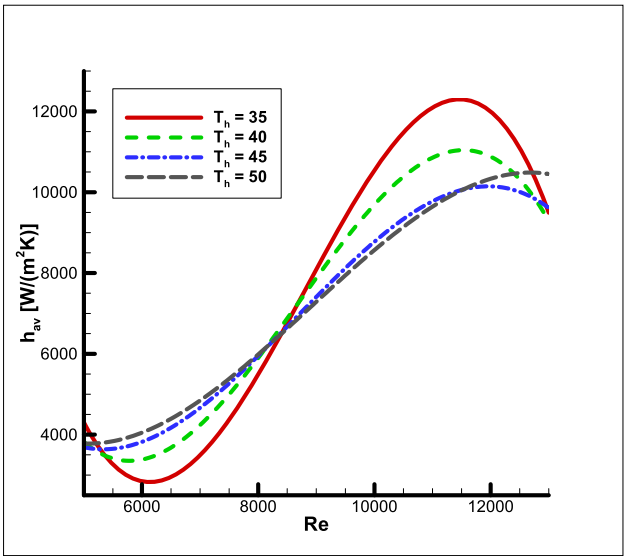

Fig. 22. Average heat transfer coefficient as a function of Reynolds number with different hot water temperatures.

Reynolds number at a hot water flow rate of $V_h =$ 0.09334 m/s and a nanofluid temperature of 15 °C at different hot water temperatures. The average heat transfer coefficient of the nanofluid increases with an increase in hot water temperature until $Re =$ 8500, where the exact opposite occurs. This is also due to the same reasons as discussed in Fig. 20.

6. Conclusion

A two-dimensional (2D) axisymmetric model of a double-pipe heat exchanger has been used to study water-based mango bark nanofluid flow. The mixture model was used and the governing equations were solved with the finite volume method. The results showed an increase of the Nusselt number and the heat transfer coefficient of the nanofluid compared to the base fluid (water) and that the Nusselt number decreased with an increase in the volume fraction and there was no optimal range of volume fraction observed for the volume fractions studied. The *LMTD* only varied by a minimal value for both fluids while that of water was higher; also the *LMTD* for nanofluids decreased with volume fraction. The effectiveness of the heat exchanger increased with volume fraction and was higher for nanofluid than for water at all Reynolds numbers studied. The average Nusselt number of the nanofluid was almost twice that of the base fluid (water) at a low Reynolds number but decreased as the Reynolds number increased for the range of Reynolds numbers studied. It was also found that there was a range of Reynolds numbers in which the trend of the average heat transfer coefficient of the nanofluid was completely reversed. More studies are recommended to understand the practical implications of the results with experimental studies for the characterized bio-material nanofluids.

Declarations

Author contribution statement

D. R. E. Ewim: Conceived and designed the experiments; Contributed reagents, materials, analysis tools or data; Wrote the paper.

E. J. Onyiriuka: Conceived and designed the experiments; Performed the experiments; Contributed reagents, materials, analysis tools or data; Wrote the paper.

A. O. Adelaja, O. O. Ighodaro: Analyzed and interpreted the data; Contributed reagents, materials, analysis tools or data; Wrote the paper.

S. Bhattacharyya: Contributed reagents, materials, analysis tools or data; Wrote the paper.

Funding statement

This research did not receive any specific grant from funding agencies in the public, commercial, or not-for-profit sectors.

Competing interest statement

The authors declare no conflict of interest.

Additional information

No additional information is available for this paper.

References

[1] Y. Cengel, Heat and Mass Transfer: a Practical Approach, McGraw-Hill, New York, 2007.
[2] S.U. Choi, J.A. Eastman, Enhancing thermal conductivity of fluids with nanoparticles, Argonne National Lab., IL (United States), 1995.
[3] W. Duangthongsuk, S. Wongwises, Heat transfer enhancement and pressure drop characteristics of TiO2–water nanofluid in a double-tube counter flow heat exchanger, Int. J. Heat Mass Transf. 52 (7-8) (2009) 2059–2067.
[4] W. Duangthongsuk, S. Wongwises, An experimental study on the heat transfer performance and pressure drop of TiO2-water nanofluids flowing under a turbulent flow regime, Int. J. Heat Mass Transf. 53 (1-3) (2010) 334–344.
[5] M. Akbari, A. Behzadmehr, Developing mixed convection of a nanofluid in a horizontal tube with uniform heat flux, Int. J. Numer. Methods Heat Fluid Flow 17 (6) (2007) 566–586.
[6] J.A. Esfahani, M. Akbarzadeh, S. Rashidi, M. Rosen, R. Ellahi, Influences of wavy wall and nanoparticles on entropy generation over heat exchanger plate, Int. J. Heat Mass Transf. 109 (2017) 1162–1171.
[7] M. Akbari, N. Galanis, A. Behzadmehr, Comparative assessment of single and two-phase models for numerical studies of nanofluid turbulent forced convection, Int. J. Heat Fluid Flow 37 (2012) 136–146.
[8] S. Kakaç, A. Pramuanjaroenkij, Review of convective heat transfer enhancement with nanofluids, Int. J. Heat Mass Transf. 52 (13-14) (2009) 3187–3196.
[9] S. Özerinç, A. Yazıcıoğlu, S. Kakaç, Numerical analysis of laminar forced convection with temperature-dependent thermal conductivity of nanofluids and thermal dispersion, Int. J. Therm. Sci. 62 (2012) 138–148.
[10] M. Pryazhnikov, A. Minakov, V.Y. Rudyak, D. Guzei, Thermal conductivity measurements of nanofluids, Int. J. Heat Mass Transf. 104 (2017) 1275–1282.
[11] B.C. Pak, Y.I. Cho, Hydrodynamic and heat transfer study of dispersed fluids with submicron metallic oxide particles, Exp. Heat Trans. 11 (2) (1998) 151–170.
[12] S. Rashidi, S. Akar, M. Bovand, R. Ellahi, Volume of fluid model to simulate the nanofluid flow and entropy generation in a single slope solar still, Renew. Energy 115 (2018) 400–410.
[13] E.J. Onyiriuka, A.I. Obanor, M. Mahdavi, D.R.E. Ewim, Evaluation of single-phase, discrete, mixture and combined model of discrete and mixture phases in predicting nanofluid heat transfer characteristics for laminar and turbulent flow regimes, Adv. Powder Technol. 29 (11) (2018) 2644–2657.
[14] E. Onyiriuka, A. Obanor, M. Mahdavi, D. Ewim, Evaluation of single-phase, discrete, mixture and combined model of discrete and mixture phases in predicting nanofluid heat transfer characteristics for laminar and turbulent flow regimes, Adv. Powder Technol. (2018).
[15] E. Onyiriuka, E. Ikponmwoba, A numerical investigation OF mango leaves-water nanofluid under laminar flow regime, Niger. J. Technol. 38 (2) (2019) 348–354.
[16] D. Wen, Y. Ding, Experimental investigation into convective heat transfer of nanofluids at the entrance region under laminar flow conditions, Int. J. Heat Mass Transf. 47 (24) (2004) 5181–5188.
[17] M. Nakhjavani, V. Nikkhah, M. Sarafraz, S. Shoja, M. Sarafraz, Green synthesis of silver nanoparticles using green tea leaves: experimental study on the morphological, rheological and antibacterial behaviour, Heat Mass Transf. 53 (10) (2017) 3201–3209.
[18] M. Sarafraz, F. Hormozi, S. Peyghambarzadeh, N. Vaeli, Upward flow boiling to DI-water and Cuo nanofluids inside the concentric Annuli, J. Appl. Fluid Mech. 8 (4) (2015).
[19] M. Sarafraz, V. Nikkhah, S. Madani, M. Jafarian, F. Hormozi, Low-frequency vibration for fouling mitigation and intensification of thermal performance of a plate heat exchanger working with CuO/water nanofluid, Appl. Therm. Eng. 121 (2017) 388–399.
[20] V. Nikkhah, M. Sarafraz, F. Hormozi, Application of spherical copper oxide (II) water nano-fluid as a potential coolant in a boiling annular heat exchanger, Chem. Biochem. Eng. Q. 29 (3) (2015) 405–415.
[21] S.Z. Heris, S.G. Etemad, M.N. Esfahany, Experimental investigation of oxide nanofluids laminar flow convective heat transfer, Int. Commun. Heat Mass Transf. 33 (4) (2006) 529–535.
[22] Y. He, Y. Jin, H. Chen, Y. Ding, D. Cang, H. Lu, Heat transfer and flow behaviour of aqueous suspensions of TiO2 nanoparticles (nanofluids) flowing upward through a vertical pipe, Int. J. Heat Mass Transf. 50 (11-12) (2007) 2272–2281.

[23] M. Lemanowicz, G. Dzido, A. Gierczycki, M. Witkowski, M. Drzazga, Numerical simulation of nanofluid flow in a small diameter pipe, Inżynieria i Aparatura Chemiczna (6) (2013) 541–542.
[24] M.K. Moraveji, M. Hejazian, CFD examination of convective heat transfer and pressure drop in a horizontal helically coiled tube with CuO/Oil base nanofluid, Numer. Heat Transf., Part A: Applications 66 (3) (2014) 315–329.
[25] M. Ahmed, M. Yusoff, K. Ng, N. Shuaib, Numerical and experimental investigations on the heat transfer enhancement in corrugated channels using SiO2–water nanofluid, Case Stud. Therm. Eng. 6 (2015) 77–92.
[26] H.E. Ahmed, M. Yusoff, M. Hawlader, M. Ahmed, Numerical analysis of heat transfer and nanofluid flow in a triangular duct with vortex generator: two-phase model, Heat Transf. Asian Res. 45 (3) (2016) 264–284.
[27] M. Saberi, M. Kalbasi, A. Alipourzade, Numerical study of forced convective heat transfer of nanofluids inside a vertical tube, Int. J. Tumor Ther. 3 (1) (2013) 10–15.
[28] V. Bianco, O. Manca, S. Nardini, Numerical investigation on nanofluids turbulent convection heat transfer inside a circular tube, Int. J. Therm. Sci. 50 (3) (2011) 341–349.
[29] M. Bahiraei, M. Hangi, Investigating the efficacy of magnetic nanofluid as a coolant in double-pipe heat exchanger in the presence of magnetic field, Energy Convers. Manag. 76 (2013) 1125–1133.
[30] L. Tabet, et al., Adverse effects of industrial multiwalled carbon nanotubes on human pulmonary cells, J. Toxicol. Environ. Health, Part A 72 (2) (2008) 60–73.
[31] M. Korani, E. Ghazizadeh, S. Korani, Z. Hami, A. Mohammadi-Bardbori, Effects of silver nanoparticles on human health, Eur. J. Nanomed. 7 (1) (2015) 51–62.
[32] N.R. Panyala, E.M. Peña-Méndez, J. Havel, Silver or silver nanoparticles: a hazardous threat to the environment and human health? J. Appl. Biomed. 6 (3) (2008).
[33] X. Chang, Y. Zhang, M. Tang, B. Wang, Health effects of exposure to nano-TiO 2: a meta-analysis of experimental studies, Nanoscale Res. Lett. 8 (1) (2013) 51.
[34] W. Qi, et al., Damaging effects of multi-walled carbon nanotubes on pregnant mice with different pregnancy times, Sci. Rep. 4 (2014) 4352.
[35] J.-M. Exbrayat, E.N. Moudilou, E. Lapied, Harmful effects of nanoparticles on animals, J. Nanotechnol. 2015 (2015).
[36] A. Tlili, J. Cornut, R. Behra, C. Gil-Allué, M.O. Gessner, Harmful effects of silver nanoparticles on a complex detrital model system, Nanotoxicology 10 (6) (2016) 728–735.
[37] I. Gosteva, Y. Morgalev, T. Morgaleva, S. Morgalev, Effect of AL2O3 and TiO2 nanoparticles on aquatic organisms, in: IOP Conference Series: Materials Science and Engineering, 98, IOP Publishing, 2015, 012007.
[38] P. Tucci, et al., Metabolic effects of TiO_2 nanoparticles, a common component of sunscreens and cosmetics, on human keratinocytes, Cell Death Dis. 4 (3) (2013) e549.
[39] M. Simonin, A. Richaume, Impact of engineered nanoparticles on the activity, abundance, and diversity of soil microbial communities: a review, Environ. Sci. Pollut. Control Ser. 22 (18) (2015) 13710–13723.
[40] M. Sharifpur, A.B. Solomon, J.P. Meyer, J. Ibrahim, E. Barki, Thermal conductivity and viscosity of Mango bark/water nanofluids. 13th International Conference on Heat Transfer, Fluid Mechanics and Thermodynamics (HEFAT2017), 2017, pp. 1022–1025.
[41] A.B. Solomon, M. Sharifpur, J.P. Meyer, J. Ibrahim, B. Immanuel, Convection Heat Transfer with Water Based Mango Bark Nanofluids, 2017.
[42] M.N. Labib, M.J. Nine, H. Afrianto, H. Chung, H. Jeong, Numerical investigation on effect of base fluids and hybrid nanofluid in forced convective heat transfer, Int. J. Therm. Sci. 71 (2013) 163–171.
[43] R. Lotfi, Y. Saboohi, A. Rashidi, Numerical study of forced convective heat transfer of nanofluids: comparison of different approaches, Int. Commun. Heat Mass Transf. 37 (1) (2010) 74–78.
[44] M.S. Mojarrad, A. Keshavarz, A. Shokouhi, Nanofluids thermal behavior analysis using a new dispersion model along with single-phase, Heat Mass Transf. 49 (9) (2013) 1333–1343.
[45] M. Manninen, V. Taivassalo, S. Kallio, On the Mixture Model for Multiphase Flow, Technical Research Centre of Finland, Finland, 1996.
[46] A. Naumann, L. Schiller, A drag coefficient correlation, Z. Ver. Deutsch. Ing. 77 (1935).
[47] M. Syamlal, W. Rogers, T.J. O'Brien, MFIX Documentation: Theory Guide, National Energy Technology Laboratory, Department of Energy, Technical Note DOE/METC-95/1013 and NTIS/DE95000031, 1993.
[48] C. Lun, S.B. Savage, D. Jeffrey, N. Chepurniy, Kinetic theories for granular flow: inelastic particles in Couette flow and slightly inelastic particles in a general flowfield, J. Fluid Mech. 140 (1984) 223–256.
[49] T.-H. Shih, W.W. Liou, A. Shabbir, Z. Yang, J. Zhu, A new k-ε eddy viscosity model for high Reynolds number turbulent flows, Comput. Fluids 24 (3) (1995) 227–238.
[50] Y. He, Y. Men, Y. Zhao, H. Lu, Y. Ding, Numerical investigation into the convective heat transfer of TiO2 nanofluids flowing through a straight tube under the laminar flow conditions, Appl. Therm. Eng. 29 (10) (2009) 1965–1972.
[51] M. Hejazian, M.K. Moraveji, A. Beheshti, Comparative numerical investigation on TiO2/water nanofluid turbulent flow by implementation of single phase and two phase approaches, Numer. Heat Transf., Part A: Applications 66 (3) (2014) 330–348.
[52] B. Kristiawan, B. Santoso, W.E. Juwana, R.M. Ramadhan, I. Riandana, Numerical investigation of laminar convective heat transfer for TiO2/water nanofluids using two-phase mixture model (Eulerian approach), in: AIP Conference Proceedings, 1788, AIP Publishing, 2017, 030002.
[53] J. Buongiorno, Convective transport in nanofluids, J. Heat Transf. 128 (3) (2006) 240–250.
[54] A. Albojamal, K. Vafai, Analysis of single phase, discrete and mixture models, in predicting nanofluid transport, Int. J. Heat Mass Transf. 114 (2017) 225–237.
[55] G.F.C. Rogers, Y.R. Mayhew, Thermodynamic and Transport Properties of Fluids, Blackwell, Oxford, 1981.
[56] B. Abedian, M. Kachanov, On the effective viscosity of suspensions, Int. J. Eng. Sci. 48 (11) (2010) 962–965.
[57] V.Y. Rudyak, A.V. Minakov, Thermophysical properties of nanofluids, Eur. Phys. J. 41 (1) (2018) 15.
[58] V. Gnielinski, New equations for heat and mass transfer in turbulent pipe and channel flow, Int. Chem. Eng. 16 (2) (1976) 359–368.